Supplementary materials

Tianyi Li[1] and Lian Shen[1] †

[1]Department of Mechanical Engineering and St. Anthony Falls Laboratory, University of Minnesota, Minneapolis, MN 55455, USA

† Email address for correspondence: shen@umn.edu

1. Validation of DNS of air turbulent Couette flow for the initialization of wind-wave generation simulation

Before conducting simulations of the coupled air–water system, we first simulate a fully developed turbulent Couette airflow by enforcing the air–water interface as a stationary non-slip boundary. In this section, we validate the DNS of turbulent Couette airflow. To confirm that the turbulent Couette airflow reaches a statistically steady state, we examine the momentum conservation equation:

$$\frac{\mathrm{d}\bar{u}^+}{\mathrm{d}z^+} - \langle u'w' \rangle^+ = 1, \tag{1.1}$$

where $\bar{u}$ denotes the mean streamwise velocity, u' and w' denote streamwise and vertical velocity fluctuations, respectively, and the superscript '+' denotes normalisation in wall units with air kinematic viscosity ν^a and air friction velocity u_τ^a. In (1.1), $\mathrm{d}\bar{u}^+/\mathrm{d}z^+$ represents the dimensionless mean viscous shear stress and $-\langle u'w' \rangle^+$ represents the dimensionless Reynolds shear stress. The summation of mean viscous shear stress and Reynolds shear stress is constant with vertical height in a statistically steady Couette flow. Figure 1 shows the plot of vertical profiles of the dimensionless mean vertical turbulent flux, mean viscous flux, and their sum. The data used to compute the plane and time averaging contains 900 different time snapshots. The sum is overall constant with height. The maximum deviation of the sum term from 1 is 0.25%, which indicates that the turbulent airflow has reached a quasi-steady state. The dashed lines (– –) in figure 1 illustrate instantaneous plane averaged Reynolds shear stress at the beginning of each independent simulations in the ensemble case (Group I). The variations among different cases indicate the unsteady and irregular nature of turbulent flows and imply the necessity to perform ensemble simulations to study the early-stage wind-wave generation problem.

We calculate the mean streamwise velocity, $\bar{u}^+$, and root mean squares of velocity fluctuations, u'^+_{rms}, v'^+_{rms}, and w'^+_{rms} in wall units, as plotted in figure 2. Our DNS results agree with other numerical and experimental studies of turbulent channel flows and Couette flows in literature. The viscous sublayer, where $\bar{u}^+ = z^+$, and the logarithmic layer, where $\bar{u}^+ = (1/0.41)\ln(\bar{z}^+) + 5.2$, are shown in figure 2($a$). Although the mean velocity profiles exhibit a similarity for the turbulent channel flows and Couette flow, the streamwise velocity fluctuation decays much faster to the centerline in the channel flows than in the Couette flows (Debusschere & Rutland 1997). Therefore, as discussed in Yang & Shen (2017), only velocity fluctuations of Couette flows in the literature are plotted in figure 2(b) for comparison.

2. Diagnostic function for determining exponential growth of surface elevation variance

In this section, we analyse the temporal growth behavior of the ensemble average of surface elevation variance $\mathbb{E}[\langle \eta^2 \rangle]$ for $tu_\tau^a/H > 50$. Figure 3(a) shows the evolution of $\mathbb{E}[\langle \eta^2 \rangle]$ in the late phase of our simulation. In figure 3(a), the x-axis and y-axis are the normal scale and logarithmic scale, respectively, and the straight line shown in figure 3(a) indicates an exponential function, i.e., $\mathbb{E}[\langle \eta^2 \rangle](t) \sim \gamma_1 \exp(\gamma_2 t)$ where γ_1 and γ_2 are constants. To further investigate the similarity between the temporal growth of surface elevation variance and an exponential function, we examine the property of its first-order derivative. For any exponential function, the ratio between its first derivative and itself is constant. Thus, we

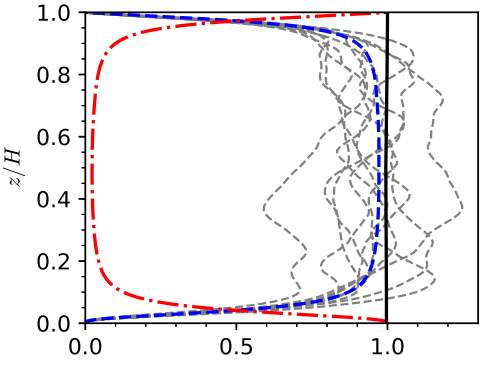

Figure 1: Profiles of Reynolds shear stress and mean viscous stress normalised in wall units: – –, Reynolds shear stress $-\langle u'w'\rangle^+$; – –, Reynolds shear stress $-\langle u'w'\rangle^+$ at $tu_\tau^a/H = 0$ for different realizations in the ensemble simulations (Group I); –·–, mean viscous stress $\mathrm{d}\bar{u}^+/\mathrm{d}z^+$; —, total stress $-\langle u'w'\rangle^+ + \mathrm{d}\bar{u}^+/\mathrm{d}z^+$.

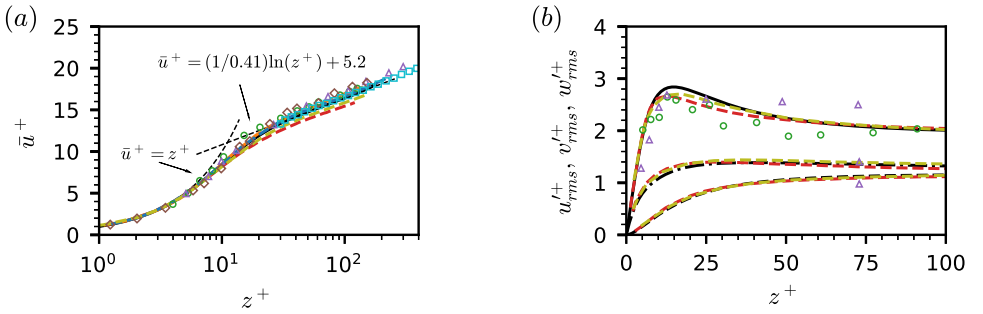

Figure 2: Profiles of (*a*) mean streamwise velocity $\bar{u}^+$ (—) and (*b*) root-mean-square velocity fluctuations (u'^+_{rms}, —; v'^+_{rms}, –·–; w'^+_{rms}, – –) normalised by the friction velocity in the air domain when the flat air–water interface is enforced to be a no-slip boundary. DNS data are plotted by dashed lines for comparison: – –, channel flow at $Re_\tau = 180$ from Kim, Moin & Moser (1987); – –, channel flow at $Re_\tau = 590$ from Moser, Kim & Mansour (1999); – –, Couette flow at $Re_\tau = 120$ from Sullivan *et al.* (2000); – –, Couette flow at $Re_\tau = 157$ from Papavassiliou & Hanratty (1997). Experimental data are plotted by symbols for comparison: ◇, channel flow at $Re_\tau = 142$ from Eckelmann (1974), which is rescaled by Kim *et al.* (1987); □, channel flow at $Re_\tau = 1000$ from Schultz & Flack (2013); △, Couette flow at $Re_\tau = 434$ from El Telbany & Reynolds (1982); ○, Couette flow at $Re_\tau = 269$ from Aydin & Leutheusser (1991). Dashed lines (– –) in (*a*) denote $\bar{u}^+ = z^+$ in the viscous sublayer and $\bar{u}^+ = (1/0.41)\ln(z^+) + 5.2$ in the logarithmic layer, respectively.

define a diagnostic function $F_3(t)$ as

$$F_3(t) = S\left(\frac{\mathrm{D_t}\,\mathbb{E}[\langle\eta^2\rangle]}{\mathbb{E}[\langle\eta^2\rangle]}\right), \tag{2.1}$$

where $\mathrm{D_t}$ is the finite difference operator of the first derivative, and S is the Savitzky–Golay filter for data smoothing. Theoretically, if the surface elevation variance grows exponentially with time, the diagnostic function F_3 is constant. As shown in figure 3(*b*), the diagnostic function F_3 overall varies slightly between 3.5 and 4.5 and has a plateau in the range $tu_\tau^a/H \in [55, 65]$. The behaviour of diagnostic function $F_3(t)$ further confirms that in the present DNS, the surface elevation variance grows exponentially with time in the late phase.

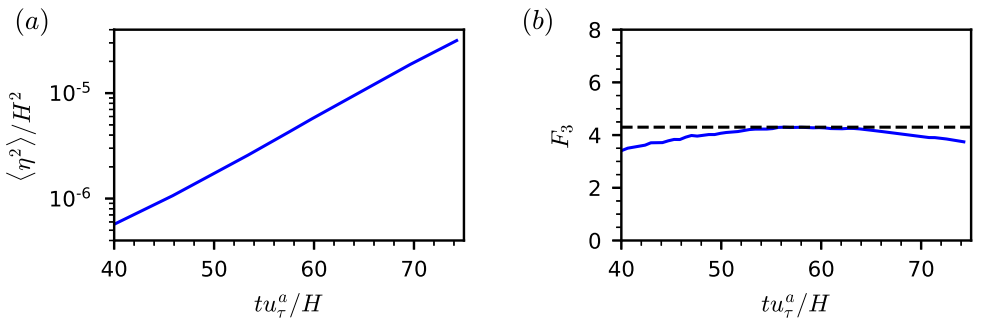

Figure 3: (*a*) Temporal evolution of surface elevation variance, normalised by the domain height H. (*b*) Temporal evolution of diagnostic function F_3 defined in equation (2.1).

3. Discussion on effects of modelling random sweeping variance term on wave growth behaviours

In this section, we discuss the alternative modelling of the variance term $\boldsymbol{k}\boldsymbol{\Sigma}\boldsymbol{k}^{\mathsf{T}}$, which is equation (4.26) in the main text. The leading order approximation of $\boldsymbol{k}\boldsymbol{\Sigma}\boldsymbol{k}^{\mathsf{T}}$ is

$$\boldsymbol{k}\boldsymbol{\Sigma}\boldsymbol{k}^{\mathsf{T}} = (k_x^2 + Ck_y^2)V_p^2, \tag{3.1}$$

where C is a constant. In the present study, the constant C is set to be 0.41 for modelling the wavenumber–frequency spectrum (Wilczek, Stevens & Meneveau 2015). We note that the choice of C value is not based on analytical derivations. Here we discuss the effect of constant C on the wave growth behaviours in the principal stage. Specifically, we analyse another model of which C is set to be 0. This alternative model can be treated as a simplification of our model proposed in the main text. We denote the model of which $C = 0.41$ as Model 1, and the alternative model of which $C = 0$ as Model 2. Thus, we have the following expressions:

$$\text{Model 1}: \quad |\boldsymbol{k}\cdot\boldsymbol{V}| = \sqrt{k_x^2 + 0.41k_y^2}V_p \tag{3.2}$$

$$\text{Model 2}: \quad |\boldsymbol{k}\cdot\boldsymbol{V}| = k_x V_p \tag{3.3}$$

The expected value of wave energy spectrum is obtained as:

$$\mathbb{E}[\widehat{\Psi}_\eta](\boldsymbol{k},t) = \frac{\sqrt{2\pi}k^2\widehat{\Pi}_p(\boldsymbol{k},0)t}{4\rho^w\Lambda^2|\boldsymbol{k}\cdot\boldsymbol{V}|}\left(\exp\left(-\frac{(\boldsymbol{k}\cdot\boldsymbol{U}-\Lambda)^2}{2(\boldsymbol{k}\cdot\boldsymbol{V})^2}\right)+\exp\left(-\frac{(\boldsymbol{k}\cdot\boldsymbol{U}+\Lambda)^2}{2(\boldsymbol{k}\cdot\boldsymbol{V})^2}\right)\right), \tag{3.4}$$

We calculate the time-dependent norm of wave energy spectrum, $\|\widehat{\Psi}_\eta(\boldsymbol{k})\|_{X_t^1}$, defined in equation (5.5) in the main text, for both Model 1 and Model 2 and compare them with the DNS results in figure 4. Model 1 has better agreements with DNS in the low-k_x and high-k_y regime of the wavenumber space than Model 2 does. In the low-k_y regime, the discrepancy between Model 1 and Model 2 is insignificant. We further show comparisons of wave growth in the principal stage among DNS results, Model 1 and Model 2 in figure 5. The variations of the upper bound and lower bound of wave linear growth rate between Model 1 and Model 2 are insignificant for both gravity–capillary waves and gravity waves. The maximum relative variation is 8% in the present DNS study. The choice of constant C does not significantly alter the modelling of the overall wave growth rate. A simple and intuitive explanation can be obtained by considering the wave energy spectrum as a continuous function of C while

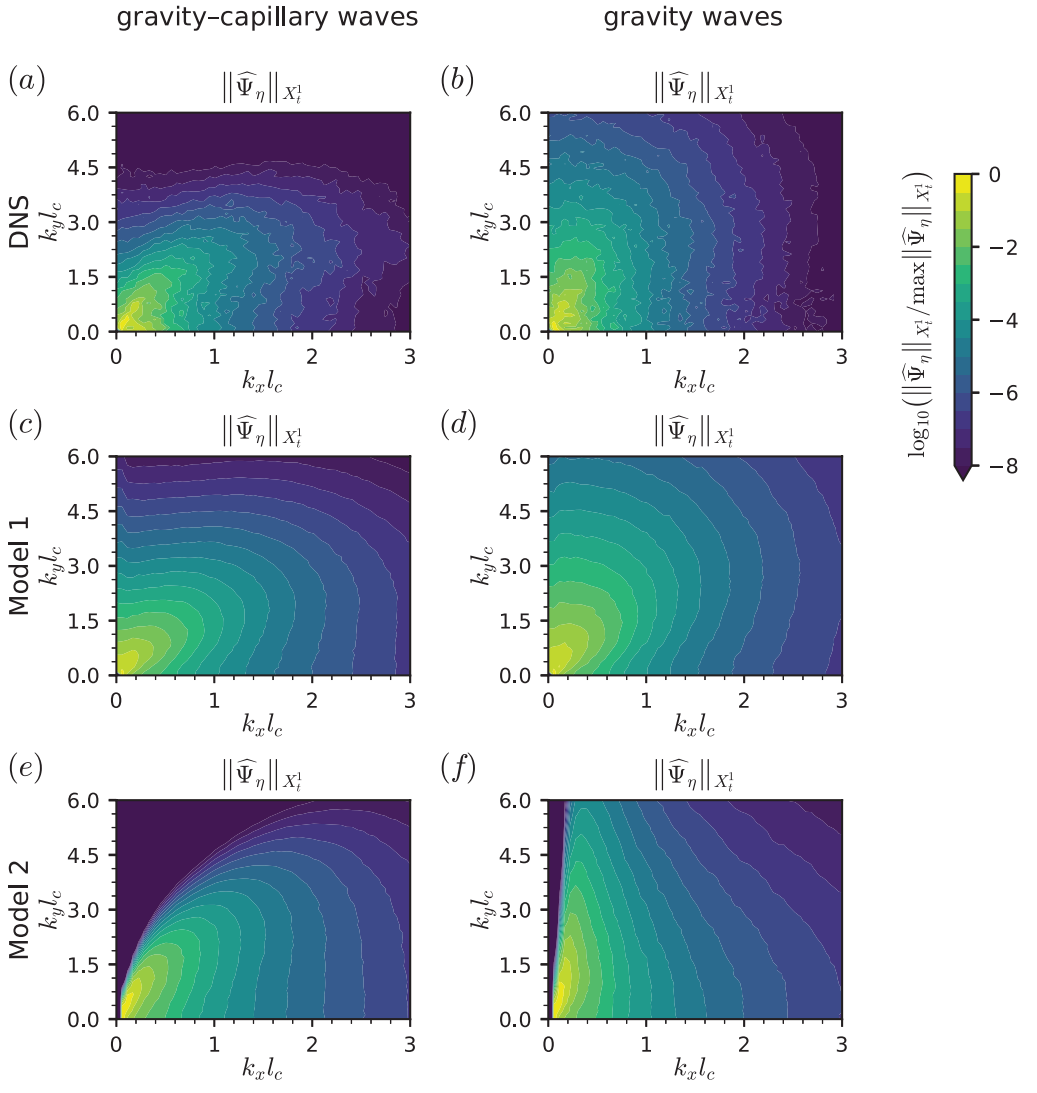

Figure 4: Comparisons of the X_t^1 norm of the wave energy spectra $\|\widehat{\Psi}_\eta\|_{X_t^1}$ in the principal stage among the DNS results, Model 1, and Model 2.

keeping other variables fixed. Therefore, the wave energy spectrum function $\mathbb{E}[\widehat{\Psi}_\eta]$ (see equation (3.4)) can be rewritten as

$$\mathbb{E}[\widehat{\Psi}_\eta](C) = \frac{\beta_1}{|\boldsymbol{k}\cdot\boldsymbol{V}|}\left(\exp\left(-\frac{\beta_2}{(\boldsymbol{k}\cdot\boldsymbol{V})^2}\right)+\exp\left(-\frac{\beta_3}{(\boldsymbol{k}\cdot\boldsymbol{V})^2}\right)\right), \tag{3.5}$$

where β_1, β_2, and β_3 are independent of C, and $|\boldsymbol{k}\cdot\boldsymbol{V}| = \sqrt{k_x^2 + Ck_y^2}V_p$. The first term on the right-hand side of (3.5), $\beta_1/|\boldsymbol{k}\cdot\boldsymbol{V}|$, is a monotonic decreasing function with respect to C, but the second term on the right-hand side of (3.5), $\exp(-\beta_2/(\boldsymbol{k}\cdot\boldsymbol{V})^2) + \exp(-\beta_3/(\boldsymbol{k}\cdot\boldsymbol{V})^2$, is a monotonic increasing function with respect to C. As a result, when C changes, the variation of $\mathbb{E}[\widehat{\Psi}_\eta]$ is not significant.

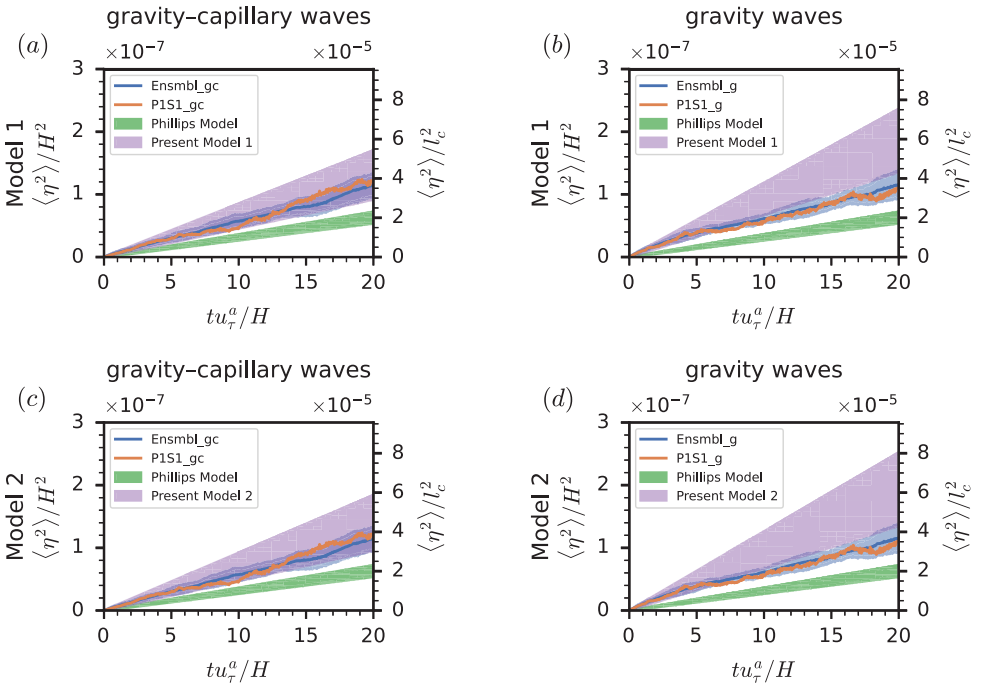

Figure 5: Comparisons of wave growth in the principal stage among the DNS results, Model 1, and Model 2 for gravity–capillary waves and gravity waves. The orange lines represent the superresolution cases (Group II). The blue lines denote the average of the ensemble cases (Group I), with the light blue shaded area being the range bounded by one standard deviation of the ensemble data. The purple and green shaded areas show the surface elevation variance predictions by the present model (Model 1 and Model 2) and the Phillips model, respectively.

REFERENCES

Aydin, E. M. & Leutheusser, H. J. 1991 Plane-Couette flow between smooth and rough walls. *Exp. Fluids* **11** (5), 302–312.

De Angelis, V., Lombardi, P. & Banerjee, S. 1997 Direct numerical simulation of turbulent flow over a wavy wall. *Phys. Fluids* **9** (8), 2429–2442.

Eckelmann, H. 1974 The structure of the viscous sublayer and the adjacent wall region in a turbulent channel flow. *J. Fluid Mech.* **65** (3), 439–459.

El Telbany, M. M. M. & Reynolds, A. J. 1982 The structure of turbulent plane Couette flow. *J. Fluids Eng.* **104**, 367–372.

Kim, J., Moin, P. & Moser, R. 1987 Turbulence statistics in fully developed channel flow at low Reynolds number. *J. Fluid Mech.* **177**, 133–166.

Moser, R. D., Kim, J. & Mansour, N. N. 1999 Direct numerical simulation of turbulent channel flow up to $Re_\tau = 590$. *Phys. Fluids* **11** (4), 943–945.

Papavassiliou, D. V. & Hanratty, T. J. 1997 Interpretation of large-scale structures observed in a turbulent plane Couette flow. *Int. J. Heat Fluid Flow* **18** (1), 55–69.

Schultz, M. P. & Flack, K. A. 2013 Reynolds-number scaling of turbulent channel flow. *Phys. Fluids* **25** (2), 025104.

Sullivan, P. P., McWilliams, J. C. & Moeng, C.-H. 2000 Simulation of turbulent flow over idealized water waves. *J. Fluid Mech.* **404**, 47–85.

Wilczek, M., Stevens, R. J. A. M. & Meneveau, C. 2015 Spatio-temporal spectra in the logarithmic layer of wall turbulence: large-eddy simulations and simple models. *J. Fluid Mech.* **769**, R1.

YANG, D. & SHEN, L. 2017 Direct numerical simulation of scalar transport in turbulent flows over progressive surface waves. *J. Fluid Mech.* **819**, 58–103.